

Machine vision-based intelligent turbulence perception for underwater wireless optical communication

Yan Jia (贾晏), Zhitong Huang (黄治同)*, Jie Xu (徐杰), Hongcheng Qiu (邱宏成), Yi Gao (高翼), and Yuefeng Ji (纪越峰)

State Key Laboratory of Information Photonics and Optical Communications (IPOC), School of Information and Communication Engineering (SICE), Beijing University of Posts and Telecommunications, Beijing 100876, China

*Corresponding author: hzt@bupt.edu.cn

Received August 29, 2024 | Accepted December 18, 2024 | Posted Online May 16, 2025

Turbulence induced by thermohaline gradient and air bubbles poses a significant challenge to the robustness of underwater wireless optical communication (UWOC) systems. It is imperative to accurately measure the turbulence intensity of the channel to guide the design of adaptive UWOC systems. However, current measurements based on pilot information consume additional spectral resources. We propose a machine vision-based intelligent turbulence perception (MV-ITP) mechanism to measure the turbulence intensity of the underwater channel. The MV-ITP mechanism utilizes the spatiotemporal intrinsic coupling correlation between optical imaging and optical communication to establish a precise quantitative relationship between the pixel intensity variation of the beam images and the scintillation index. We conduct experiments under different turbulence conditions induced by temperature, salinity, as well as air bubbles, and the experimental results demonstrate that the proposed mechanism can accurately measure the intensity of turbulence.

Keywords: turbulence intensity; machine vision; underwater wireless optical communication.

DOI: [10.3788/COL202523.060601](https://doi.org/10.3788/COL202523.060601)

1. Introduction

Underwater wireless communication, which transmits information in the underwater environment through wireless carriers, has greatly facilitated the development of underwater exploration activities. Due to the high delays of underwater acoustic communication and the high attenuation of underwater radio-frequency communication, underwater wireless optical communication (UWOC) emerges as a more promising technology because of its lower costs, stronger anti-interference capabilities, and richer spectrum resources^[1,2].

However, the UWOC system faces a significant challenge due to underwater optical turbulence (UOT), which stems from the presence of a thermohaline gradient and air bubbles in the underwater environment. Specifically, in the marine environment, a thermohaline gradient is widespread due to the ocean currents and the melting of fresh water from glaciers. Air bubbles are generated by the decomposition of marine life, inorganic matter, and leakage from undersea gas fields. UOT leads to rapid fluctuations of the water refractive index, resulting in the intensity fluctuations of received signals, ultimately degrading the performance of UWOC systems^[3].

To comprehend the effects of UOT on optical signal propagation, recent studies have investigated the statistical

distribution of optical signal fluctuations under the influence of UOT. Jamali *et al.* conducted experimental research to compare the fitting goodness of various single-peak statistical distributions in the UWOC channel under the influence of air bubbles, temperature, and salinity random variations^[4]. Zedini *et al.* proposed the mixture exponential-generalized gamma distribution to characterize the effect of turbulence on channel irradiance fluctuations in both fresh and saltwater environments^[5]. Moreover, Bernotas *et al.* associated the channel statistical model with the scintillation index (SI)^[6]. Qiu *et al.* proposed the unified Weibull-generalized gamma distribution to characterize the statistics of the laser beam irradiance fluctuations and derived the expression for the SI^[7]. Therefore, SI is a key parameter for assessing the impact of turbulence on the optical signals and measuring the fluctuations in the optical signal. To understand the effect of turbulence on UWOC, it is necessary to obtain the SI of the channel.

However, in current measurement mechanisms, the insertion of pilot information occupies a certain transmission bandwidth and decreases spectrum efficiency. Zeyad *et al.* showed that the pilot-assisted technique suffered from the deterioration of spectral efficiency due to the transmitted side information in UWOC systems^[8]. To detect the channel state information, a pilot symbol needs to be added to the signal, which decreases the

spectrum efficiency^[9,10]. To solve this problem, we consider introducing machine vision into UWOC, which has been used as a technique to assist in channel perception. Dong *et al.* utilized machine vision to establish the relationship between bubble density and SI, enabling prediction of bubble effects on received signals in advance^[11]. Huang *et al.* developed a mechanism for obtaining channel quality by analyzing captured images and proposed the spatiotemporal intrinsic coupling correlation between optical imaging and optical communication^[12]. Moreover, several studies have shown that UOT affected imaging quality. Oubei *et al.* demonstrated that the received beam images were distorted due to underwater turbulence through experiments^[13]. Yuan *et al.* experimentally explored the microscopic characteristics of the laser beam propagation influenced by turbulence^[14–16]. Therefore, we consider utilizing the inherent relationship between optical imaging and optical communication to obtain the SI from images. By capturing images of the laser beam propagation in the communication link and analyzing SI, we could understand the impact of underwater turbulence on communication and design a more intelligent UWOC system.

In this Letter, we propose a machine vision-based intelligent turbulence perception (MV-ITP) mechanism in the UWOC system. The MV-ITP mechanism utilizes a camera to capture real-time images of beam propagation in the channel, from which the SI of signal strength fluctuations caused by underwater turbulence can be obtained. This is crucial for accurately understanding the effects of turbulence on UWOC systems.

2. Principle of MV-ITP Mechanism

Figure 1 presents the block diagram of the proposed MV-ITP mechanism. The optical transceivers are used to transmit and receive signals. A steady reference beam emitted by transceiver

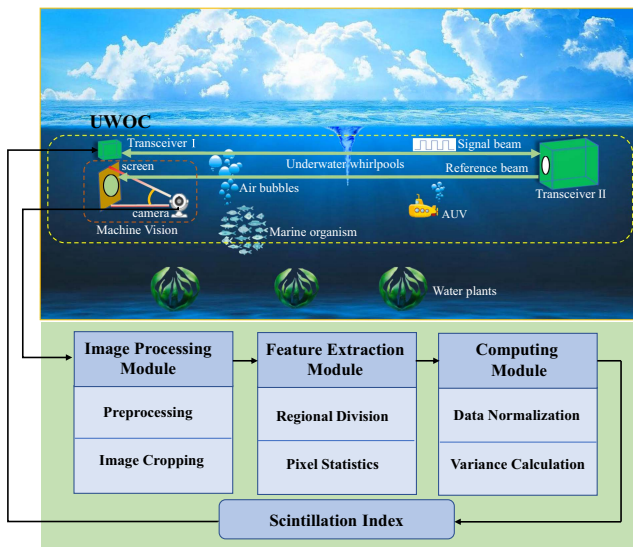


Fig. 1. Block diagram of the MV-ITP mechanism. AUV, autonomous underwater vehicle.

II is used to measure the turbulence intensity. Based on the reciprocity of underwater channels, the beam emitted from transceiver II can offer channel state information^[17]. The camera placed at transceiver I end is used to capture real-time images of the beam. The captured videos will go through an image-processing module, a feature extraction module, and a computing module in turn. Eventually, the SI will be derived to help the transceiver obtain the intensity of turbulence.

In the image-processing module, the video undergoes a pre-processing operation to be segmented into individual frames. To extract precise features, square pixel blocks of suitable size are chosen within the nonedge area of the spot. The pixel block size is determined by the size of the light spot, aiming to encompass as much information about the spot as possible while minimizing the inclusion of pixels outside the edges. Then the images are cropped to a resolution of $l \times l$ size and forwarded to the subsequent module.

In the feature extraction module, the flickering characteristics of the beam are reflected in the intensity of the pixels in different regions of the images. We divide the cropped images into smaller regions so that the variation in pixel intensity is accurately obtained. Specifically, we define a local window with a resolution of $s \times s$ as the smallest statistical unit, and each image consists of $m \times m$ local windows ($l = s \times m$). The matrix $\mathbf{I}_{s \times s}$ consisting of all pixel values in a local window is shown as follows:

$$\mathbf{I}_{s \times s} = \begin{bmatrix} I_{11} & I_{12} & \cdots & I_{1s} \\ I_{21} & I_{22} & \cdots & I_{2s} \\ \cdots & \cdots & \cdots & \cdots \\ I_{s1} & I_{s2} & \cdots & I_{ss} \end{bmatrix}. \quad (1)$$

In order to observe the changes in the beam images experiencing turbulence, we obtain a reference interval of pixels from a still-water environment. We define the reference interval as the range of pixel values within which more than 90% of the pixels are counted, starting from the highest pixel value in the received beam image. It is denoted as $[I_{low}, I_{high}]$, where I_{high} and I_{low} represent the maximum pixel value and the minimum pixel value, respectively. When the beam emitted by the transmitter encounters turbulence, the distribution of pixel values in each local window may vary. We denote the number of pixels with pixel values within the reference range in the local window located in row $x + 1$ and column $y + 1$ as $N(x, y)$, which is expressed as

$$N(x, y) = \sum_{i=1}^s \sum_{j=1}^s \mathbb{I}(I_{low} \leq |I_{ij}| \leq I_{high}), \quad (2)$$

where \mathbb{I} denotes the indicator function, which takes the value 1 when the condition is satisfied. I_{ij} is the element of the row i and column j of the matrix $\mathbf{I}_{s \times s}$. Then the number of pixels within the reference range in all local windows is represented by the matrix $\mathbf{N}_{m \times m}$, which is given by

$$\mathbf{N}_{m \times m} = \begin{bmatrix} N(0, 0) & N(0, 1) & \cdots & N(0, m-1) \\ N(1, 0) & N(1, 1) & \cdots & N(1, m-1) \\ \cdots & \cdots & \cdots & \cdots \\ N(m-1, 0) & \cdots & \cdots & N(m-1, m-1) \end{bmatrix}. \quad (3)$$

In the computing module, we calculate the data collected by the feature extraction module to derive the SI. The SI (denoted by σ_I^2), which is commonly used in the literature to measure the strength of turbulence^[18], is defined as the normalized variance of intensity fluctuations and is given by

$$\sigma_I^2 \triangleq \frac{\mathbb{E}[I^2] - \mathbb{E}[I]^2}{\mathbb{E}[I^2]}, \quad (4)$$

where \mathbb{E} denotes the expected value and I represents the generated normalized current of the photodiode (PD). The generated current of PD serves as a representation of the received irradiance, as its output current is proportional to the received optical power in its linear region.

To obtain the $\hat{S}I$ captured in images, we calculate the normalized variances of the number of pixels counted in each local window, which are at the same location in consecutive k frames of the images. Taking the local window of the first row and first column as an example, the detailed calculation process is as follows. First, the k consecutive frames are represented by the vector $\mathbf{n}(0, 0)$ with the formula,

$$\mathbf{n}(0, 0) = [N_0(0, 0), N_1(0, 0), \cdots, N_{k-1}(0, 0)]. \quad (5)$$

Then the maximum value of the k elements is denoted as $N_{\max}(0, 0)$ and the minimum value as $N_{\min}(0, 0)$, and the data normalization method is given by

$$N'_z(0, 0) = \frac{N_z(0, 0) - N_{\min}(0, 0)}{N_{\max}(0, 0) - N_{\min}(0, 0)}, \quad (6)$$

where $N'_z(0, 0)$ denotes the normalized data in the $(z + 1)$ _{th} frame. Finally, the normalized data are used to calculate the variance:

$$\hat{\sigma}_{N'(0,0)}^2 = \frac{\mathbb{E}[N'^2(0, 0)] - \mathbb{E}[N'(0, 0)]^2}{\mathbb{E}[N'(0, 0)]^2}, \quad (7)$$

where \mathbb{E} denotes the expected value calculated from the images. To minimize the random error, we average the normalized variances obtained from all local windows to get the final $\hat{S}I$, which is given by

$$\hat{S}I = \frac{\sum_{r=0}^{m-1} \sum_{w=0}^{m-1} \hat{\sigma}_{N'(r,w)}^2}{m^2}, \quad (8)$$

where r represents the row $r + 1$ and w represents the column $w + 1$.

In order to validate the accuracy of the proposed mechanism, we introduce the metric root mean square error (RMSE), which

is a commonly used measure of the difference between values, given by

$$\text{RMSE} = \sqrt{\frac{\sum_{a=1}^n (\hat{y}_a - y_a)^2}{n}}, \quad (9)$$

where \hat{y} stands for the results based on image data, y represents the results based on PD sampling data, and n represents the number of data. If $\hat{S}I$ obtained from the machine vision-based method matches SI calculated from PD sampling data, we can utilize the machine vision-based method to derive the SI in a more flexible way.

3. Experiments and Result Analysis

In this section, we present the experimental setup and analyze the results. Figure 2 illustrates the experimental setup used to measure the SI in the UWOC system under the influence of turbulence. The water tank, with dimensions of $0.1 \text{ m} \times 0.2 \text{ m} \times 1 \text{ m}$, is wrapped with black stickers to minimize interference from light reflected from the sidewalls of the tank. Tap water is used to emulate seawater due to their similar attenuation coefficients^[19]. At the transmitter end, a 450 nm blue laser diode (LD) is driven by a direct current (DC) power supply. A heating rod is placed in the water tank to create a temperature gradient. Three thermometers are placed at the transmitter end, the middle of the tank, and the receiver end to detect the water temperature in real time. An air pump placed in the middle of the water tank is used to generate air bubbles which have a flow rate range of 0–15 L/min.

Different concentrations of salt water are slowly added to Input I and Input II to create a salinity gradient. At the receiver side, the beam is captured by a PIN PD with an active area diameter of $800 \mu\text{m}$ and a camera, respectively. The PD's generated current is sampled by a 3.5 GHz bandwidth oscilloscope with a sampling rate of 5 kSa/s. The resolution of the camera is 1080 p and the rate is 30 frame/s (fps). All experimental data are taken under no room illumination conditions, and the images are processed on a personal computer (PC).

We conduct two sets of experiments to investigate the optical beam irradiance fluctuations under various underwater turbulence scenarios. The first set of experiments simulates the effect

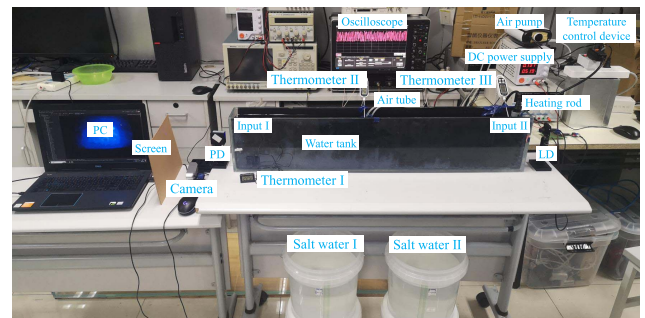


Fig. 2. Experimental setup.

of the thermohaline gradient. Initially, we add tap water to the tank to a height of 12 cm. The temperature of the water is 15°C. Then the water temperature at the transmitter end is heated to 25°C or 35°C to create a temperature gradient of 0.1 or 0.2°C/cm. 2 L of salt water with a concentration of 120 g/L is added to Input 1 and 2 L of salt water with a concentration of 160 g/L is added to Input 2 to produce a salinity gradient of 0.1 g/(L · cm). To produce a salinity gradient of 0.2 g/(L · cm), the concentrations of salt water added are 100 and 180 g/L, respectively. Nine different thermohaline gradients are ultimately created, and it is noteworthy that the average salinity in each scenario is 35 g/L. We collect 50,000 PD-generated current samples under nine thermohaline gradients. Additionally, we capture 300 consecutive frames of images using a camera under each condition. Based on the size of the beam in the video, the images are cropped into squares with a resolution of 220 × 220.

Figure 3 shows typical images captured by the camera after cropping under different thermohaline gradients. In the four turbulence scenarios shown in Fig. 3, noncontiguous images are selected from 300 frames of images. We calculate the average pixel values of the blue channel for the images. When the temperature gradient is 0°C/cm and the salinity gradient is 0 g/(L · cm), the images are almost identical and the pixel average value is the highest. As the turbulence intensity increases, the average value of the blue channel pixel decreases, indicating an increase in attenuation of the optical imaging signal.

Figure 4 shows typical waveform plots from the oscilloscope and typical cropped images for nine different thermohaline gradients. As the temperature gradient and the salinity gradient

Turbulence Scenario	Typical Images				Pixel Average Value
Gr: 0 °C/cm Gs: 0 g/(L · cm)					247.29
Gr: 0.2 °C/cm Gs: 0 g/(L · cm)					244.36
Gr: 0 °C/cm Gs: 0.2 g/(L · cm)					244.50
Gr: 0.2 °C/cm Gs: 0.2 g/(L · cm)					243.79

Fig. 3. Typical cropped images under four different thermohaline gradients.

Temperature Gradient (°C/cm) \ Salinity Gradient (g/(L · cm))	0			0.1			0.2		
	Waveform	Image	Pixel Average Value	Waveform	Image	Pixel Average Value	Waveform	Image	Pixel Average Value
0			247.24			246.06			244.66
0.1			245.83			243.04			241.84
0.2			240.47			239.82			238.77

Fig. 4. Typical waveforms and typical images under nine different thermohaline gradients.

increase, the signal fluctuates significantly, and the maximum value of the signal amplitude shows a downward trend. Moreover, the average pixel value of the images decreases as the strength of turbulence increases.

In the feature extraction module, we set the size of the local window to 22 × 22, meaning that a cropped image contains 100 local windows. In the cropped image of size 220 × 220, more than 90% of the pixel values fall within the range of [245, 255], which is defined as the reference range. For the same local window, we count the number of pixels within the reference range in 300 consecutive frames.

In the computing module, the normalized variance is calculated using Eq. (7). Finally, the data obtained from 100 local windows are averaged; this is the \hat{SI} we obtain from the machine vision-based method. The histogram depicting the variation of the SI obtained by the two methods versus the thermohaline gradient is presented in Fig. 5.

The SIs obtained by the two methods are both small when the channel is not affected by turbulence. As the turbulence increases, SI increases because greater fluctuations are induced in the received signal. Moreover, the superposition of the two factors further amplifies the signal fluctuation, surpassing the effect of a single factor. After calculation, the RMSE of the two methods is 0.015, which is close to 0, indicating that the proposed mechanism is accurate.

The second set of experiments simulates the effects of air bubbles and the temperature gradient. In this set of experiments, we verify the presence of only bubbles and the simultaneous presence of bubbles and temperature gradients. We add water to the tank up to 16 cm. At the bubble rate of 0–15 L/min, 50,000 PD sampling current data are recorded by an oscilloscope and 300 consecutive frames of images are recorded by a camera, with the bubble rate incremented by 1 L/min each time. The temperature gradient is introduced in the same way as in the first set of experiments. When the temperature gradient is 0.1°C/cm, we turn on the air pump and collect data from the oscilloscope and the camera under bubble rates ranging from 0 to 15 L/min.

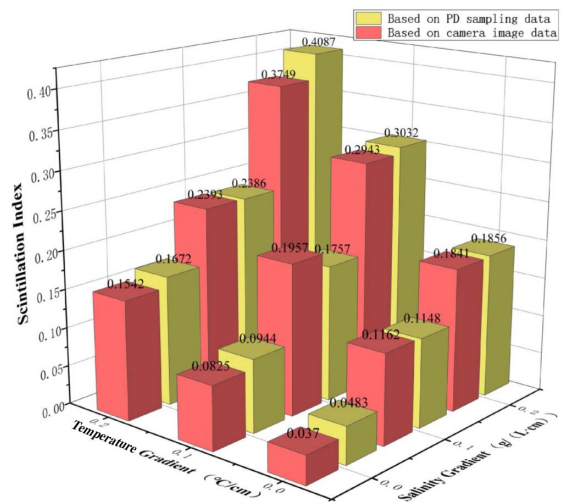


Fig. 5. Histogram of scintillation index for nine thermohaline gradients.

Figure 6 shows typical cropped images at the bubble rates of 0, 5, 10, and 15 L/min. As the bubble rate increases, the difference between different images for the same turbulent condition becomes progressively larger. In addition, the average pixel value decreases as the turbulence intensity increases, indicating an increase in attenuation of the optical imaging signal. It is worth noting that the appearance of dark pixels at the edge of the cropped images is caused by the beam drift and occlusion.

Figure 7 shows typical images under different bubble rates when the temperature gradient is 0.1°C/cm. Compared to the case where no temperature gradient is introduced, e.g., when the bubble rate is 5 L/min, beam drift is increased and dark pixel regions at the image edges are increased, indicating the degradation of the imaging quality.

As shown in Fig. 8, we select typical waveform graphs conducted at the bubble rates of 0, 5, 10, and 15 L/min. As the bubble rate increases, the points where the sampling current decays to 0 or close to 0 increase significantly, indicating a higher probability of the communication link being obscured.

Figure 9 shows the $\hat{S}I$ and SI after feature extraction and computing.

The $\hat{S}I$ and SI increase as the bubble rate increases. Moreover, the results increase with the addition of a 0.1°C/cm temperature gradient, indicating that the combination of the two factors amplifies turbulence intensity. The RMSEs of the two data sets are 0.0227 and 0.0285, respectively, verifying the accuracy of the proposed mechanism.

Turbulence Scenarios	Typical Images	Pixel Average Value
Rx : 0 L/min		247.29
Rx : 5 L/min		234.01
Rx : 10 L/min		211.46
Rx : 15 L/min		200.98

Fig. 6. Typical images under four different bubble rates.

Turbulence Scenarios	Typical Images	Pixel Average Value
Gr : 0.1 °C/cm Rx : 0 L/min		245.48
Gr : 0.1 °C/cm Rx : 5 L/min		225.69
Gr : 0.1 °C/cm Rx : 10 L/min		212.87
Gr : 0.1 °C/cm Rx : 15 L/min		211.02

Fig. 7. Typical images under different bubble rates when the temperature gradient is 0.1°C/cm.

Bubble Rate (L/min)	Temperature Gradient (°C/cm)	
	0	0.1
0	 Pixel Average Value 247.01	 Pixel Average Value 246.29
5	 Pixel Average Value 220.38	 Pixel Average Value 229.38
10	 Pixel Average Value 214.95	 Pixel Average Value 216.19
15	 Pixel Average Value 205.66	 Pixel Average Value 201.84

Fig. 8. Typical waveforms and typical images under different temperature gradients and different bubble rates.

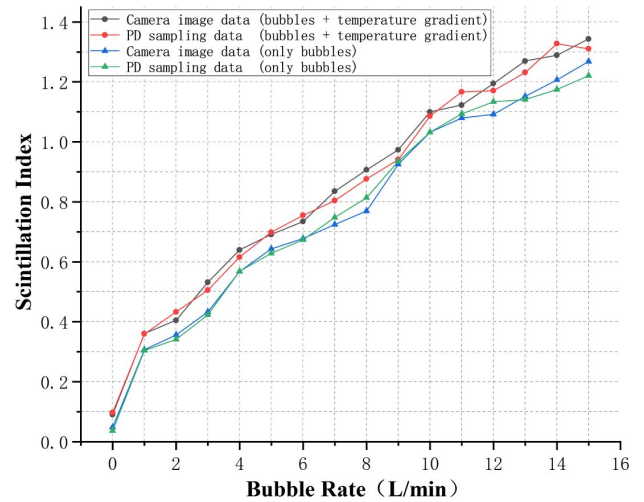


Fig. 9. Scintillation indices under different bubble rates and different temperature gradients.

Based on the proposed mechanism, the $\hat{S}I$ can be obtained and further sent to the transceiver. This is significant for understanding the state of the channel. In our future work, to increase the accuracy of the mechanism, we will introduce artificial intelligence techniques to extract the scintillation characteristics of the images.

4. Conclusion

In this paper, we proposed an MV-ITP mechanism for underwater turbulence intensity measurement in the UWOC system. The MV-ITP mechanism establishes a precise quantitative relationship between the pixel intensity variation of the beam images and the scintillation index. The accuracy of the proposed mechanism is validated through emulated experiments under

various turbulent channel conditions induced by a thermohaline gradient and air bubbles. By monitoring the turbulence intensity of the channel, the mechanism helps the transceiver sense the channel state, which has great significance for developing robust and flexible UWOC systems.

Acknowledgements

This work was supported by the National Natural Science Foundation of China (No. 62371058) and the Beijing Municipal Natural Science Foundation (No. L232048).

References

1. Z. Zeng, S. Fu, H. Zhang, *et al.*, "A survey of underwater optical wireless communications," *IEEE Commun. Surv. Tutorials* **19**, 204 (2017).
2. X. Sun, C. H. Kang, M. Kong, *et al.*, "A review on practical considerations and solutions in underwater wireless optical communication," *J. Light. Technol.* **38**, 421 (2020).
3. I. C. Ijeh, M. A. Khalighi, M. Elamassie, *et al.*, "Outage probability analysis of a vertical underwater wireless optical link subject to oceanic turbulence and pointing errors," *J. Opt. Commun. Netw.* **14**, 439 (2022).
4. M. V. Jamali, A. Mirani, A. Parsay, *et al.*, "Statistical studies of fading in underwater wireless optical channels in the presence of air bubble, temperature, and salinity random variations," *IEEE Trans. on Commun.* **66**, 4706 (2018).
5. E. Zedini, H. M. Oubei, A. Kammoun, *et al.*, "Unified statistical channel model for turbulence-induced fading in underwater wireless optical communication systems," *IEEE Trans. Commun.* **67**, 2893 (2019).
6. M. P. Bernotas and C. Nelson, "Probability density function analysis for optical turbulence with applications to underwater communications systems," *Proc. SPIE* **9827**, 98270D (2016).
7. H. Qiu, Z. Huang, J. Xu, *et al.*, "Unified statistical thermocline channel model for underwater wireless optical communication," *Opt. Lett.* **48**, 636 (2023).
8. Z. A. H. Qasem, A. Ali, B. Deng, *et al.*, "Spectral and energy efficient pilot-assisted PAPR reduction technique for underwater wireless optical communication systems," *J. Light. Technol.* **42**, 841 (2024).
9. H. Lu, M. Jiang, and J. Cheng, "Deep learning aided robust joint channel classification, channel estimation, and signal detection for underwater optical communication," *IEEE Trans. Commun.* **69**, 2290 (2021).
10. A. Kumar, S. Al-Kuwari, D. N. K. Jayakody, *et al.*, "Security performance analysis of a NOMA-assisted underwater VLC system under imprecise channel estimations," *IEEE Access* **10**, 117021 (2022).
11. Z. Dong, Z. Huang, H. Qiu, *et al.*, "Bubbles-induced turbulence channel prediction mechanism based on machine vision in underwater wireless optical communication," *Opt. Express* **31**, 40469 (2023).
12. Z. Huang, L. Zu, Z. Zhou, *et al.*, "Computer-vision-based intelligent adaptive transmission for optical wireless communication," *Opt. Express* **27**, 7979 (2019).
13. H. M. Oubei, X. Sun, T. K. Ng, *et al.*, "Scintillations of RGB laser beams in weak temperature and salinity-induced oceanic turbulence," in *2018 Fourth Underwater Communications and Networking Conference (UComms)* (2018), p. 1.
14. R. Yuan, J. Sun, T. Luo, *et al.*, "Simulation study on light propagation in an anisotropic turbulence field of entrainment zone," *Opt. Express* **22**, 13427 (2014).
15. R. Yuan, J. Sun, T. Luo, *et al.*, "Simulation study on light propagation in an isotropic turbulence field of the mixed layer," *Opt. Express* **22**, 7194 (2014).
16. Y. Renmin, M. Jie, L. Hao, *et al.*, "Simulation of the microstructural characteristics of saltwater turbulence in a water tank," *Opt. Express* **26**, A844 (2018).
17. Y. Guo, A. Trichili, O. Alkhazragi, *et al.*, "On the reciprocity of underwater turbulent channels," *IEEE Photonics J.* **11**, 1 (2019).
18. W. Liu, Z. Xu, and L. Yang, "SIMO detection schemes for underwater optical wireless communication under turbulence," *Photon. Res.* **3**, 48 (2015).
19. J. W. Giles and I. N. Bankman, "Underwater optical communications systems. Part 2: basic design considerations," in *MILCOM 2005-2005 IEEE Military Communications Conference* (2005), p. 1700.